Front. Struct. Civ. Eng. 2024, 18(2): 252–271
https://doi.org/10.1007/s11709-024-1059-1

RESEARCH ARTICLE

Experimental study of face passive failure features of a shallow shield tunnel in coastal backfill sand

Weifeng QIAN[a], Ming HUANG[a*], Bingnan WANG[a], Chaoshui XU[b], Yanfeng HU[c]

[a] *School of Civil Engineering, Fuzhou University, Fuzhou 350108, China*
[b] *School of Civil, Environment and Mining Engineering, University of Adelaide, Adelaide 5005, Australia*
[c] *China First Highway Xiamen Engineering Co., Ltd., Xiamen 361000, China*
[*] *Corresponding author. E-mail: huangming05@fzu.edu.cn*

ABSTRACT Face passive failure can severely damage existing structures and underground utilities during shallow shield tunneling, especially in coastal backfill sand. In this work, a series of laboratory model tests were developed and conducted to investigate such failure, for tunnels located at burial depth ratios for which C/D = 0.5, 0.8, 1, and 1.3. Support pressures, the evolution of failure processes, the failure modes, and the distribution of velocity fields were examined through model tests and numerical analyses. The support pressure in the tests first rose rapidly to the elastic limit and then gradually increased to the maximum value in all cases. The maximum support pressure decreased slightly in cases where C/D = 0.8, 1, and 1.3, but the rebound was insignificant where C/D = 0.5. In addition, the configuration of the failure mode with C/D = 0.5 showed a wedge-shaped arch, which was determined by the outcropping shear failure. The configuration of failure modes was composed of an arch and the inverted trapezoid when C/D = 0.8, 1, and 1.3, in which the mode was divided into lower and upper failure zones.

KEYWORDS tunnel face stability, passive failure, model test, support pressure, failure mode

1 Introduction

With increasing urbanization, shield tunneling is mostly used in underground traffic infrastructure construction on account of its characteristic safety and efficiency [1,2]. The stability of tunnel faces is a key quality and safety factor during construction [3,4]. Calculating an appropriate support pressure is crucial for maintaining the stability of tunnel faces [5], and inadequate or excessive support pressure may cause active or passive failures [6]. The active failure of tunnel faces has been extensively investigated [7–9], but reports of passive failure remain much rarer [10–12]. The tunneling direction of shield machines is the front of tunnel faces during shield tunneling. When passive failure of the face occurs, the soil in front of the face is pushed toward the ground surface, which leads to ground surface uplift and tunnel face blow-out [13]. In The Netherlands, on the 2nd Heinenroord Tunnel project, a passive failure of the face was generated when drilling through a sand stratum [14]. In the Guangzhou Metro Line 1, Peasant Movement Institute Station to Martyrs' Park Station, the shield machine set an excessive total thrust in silty clay strata, leading to severe ground surface uplift [15]. The main reason for these construction accidents is a lack of knowledge of the mechanisms of passive failure, justifying the present work.

In practice, according to the technical code stipulated by Ref. [16], the condition that the burial depth of the tunnel exceeds its diameter should be satisfied to prevent the passive failure of tunnel faces. However, in recent decades, shallow shield tunnels have become prevalent, and significantly decreased burial depth has increased the risk of passive failure of tunnel faces [17]. A typical example can be found in the Xiamen Metro, Line 3 Shuanghu Station to Airport Economic Zone Station (metro tunnel), which is a shallow shield tunnel located in a coastal backfill sand stratum, in Fujian Province, China (Fig. 1). The metro tunnel utilized an earth pressure balance shield machine crossing the coastal backfill sand

Article history: Received Apr 30, 2023; Accepted Aug 27, 2023

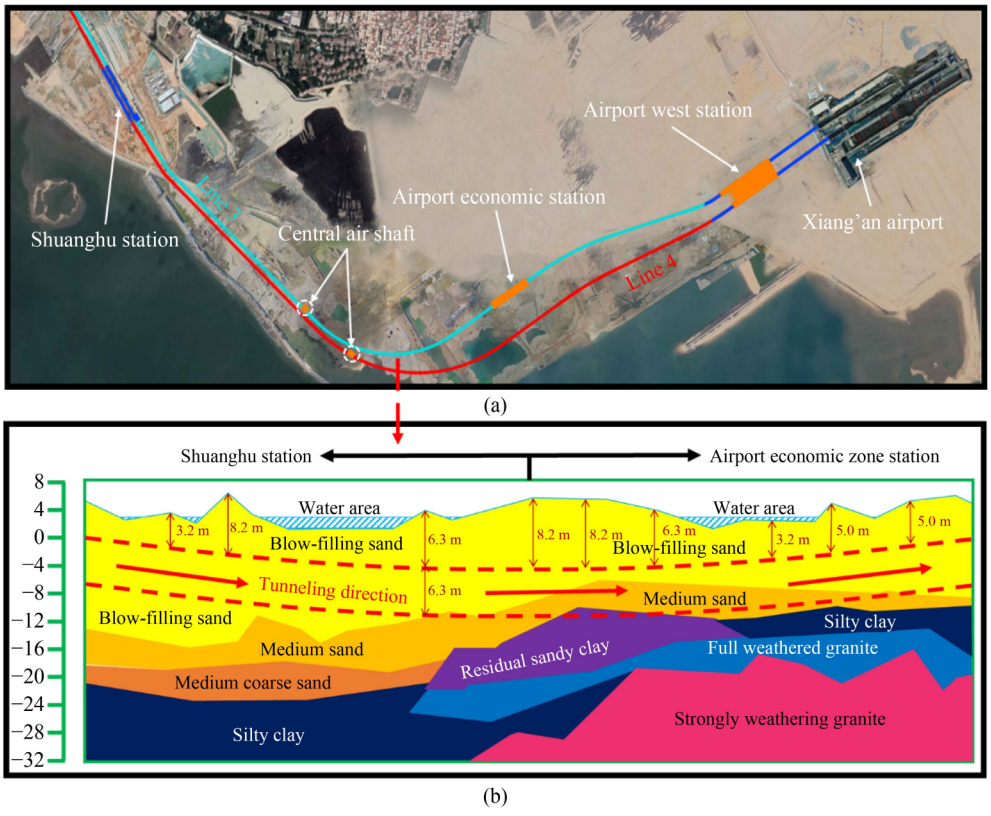

Fig. 1 *In situ* conditions: (a) Aerial view of Shuang-Airport shield zone; (b) longitudinal geological strata profile.

stratum with a diameter of 6.3 m; the soil cover thickness of shield tunnels ranged from 3.2 to 8.2 m. Backfilled sand is widely distributed in areas of coastal reclamation lands; this material is characterized by its loose structure, low shear strength, and poor bearing capacity [18]. Without a doubt, a shallow tunnel face in such conditions is susceptible to passive failure. Hence, many scholars have used theoretical analyses, experimental tests, and numerical simulations to ascertain the failure mode and determine the required support pressure for ensuring the stability of the tunnel face.

Theoretical analyses, including the limit equilibrium method [19–28] and the limit analysis method [29–38], were used to evaluate the tunnel face stability. Li et al. [38] investigated the influence of non-associated flow rules on the passive face instability for shallow shield tunnels using the upper bound method from the limit analysis. Di et al. [39,40] analyzed face stability, for tunnels under seepage flow in the saturated ground, based on the three-dimensional hydraulic head distribution model and the upper bound theorem. However, the theoretical model relied on several essential assumptions, particularly regarding the failure mode, which led the model result to deviate from reality. Compared with the theoretical method, numerical simulation may be a more effective technique for face stability analysis due to its superior computational efficiency. Some academics have explored the stability of tunnel faces under different working conditions using numerical simulation, mainly including finite element methods [41–43], finite difference methods [35,38,44], and discrete element methods [45–47]. It is noteworthy that the numerical simulation in those cases was dependent on the material model and the material parameter, and the numerical result should be corroborated by other methods. At this point, an experimental study offers a useful approach to exploring failure modes and verifying theoretical and numerical results.

Most laboratory experiments on tunnel face stability fall into two categories, which are centrifuge model tests [10,11,48–50] and 1–g model tests [7,51,52,56,57]. The centrifuge model tests have only been conducted at a few research institutes due to the high technical requirements of the experimental equipment. As instrumentation equipment and measurement techniques have improved, 1–g model tests have been developed to simulate more complicated geometries and construction conditions. The 1–g model tests, also known as conventional gravity model tests, have included large-scale and small-scale model tests. Berthoz et al. [52] employed 1–g large-scale model tests to compare data on the ultimate support pressure of tunnel faces with theoretical predictions. Chen et al. [7] applied a load cell and linear variable differential transducer in large-scale model tests to study failure mechanism. Di et al. [53–55] adopted the large-scale experiment platform to research the instability characteristics of

tunnel faces in sandy cobble strata with different densities. Although the 1–g large-scale model tests have many advantages, the experiment platform is expensive and occupies a larger space. Many institutes with limited scientific research facilities have focused on the small-scale model test. Kirsch [51] explored tunnel face stability by 1–g small-scale model tests and introduced particle image velocimetry (PIV) to trace the routes of sand particles. Liu et al. [9] studied the influence of the velocity of the support plate on the extent of the active failure mode in dense sand. Cheng et al. [56] carried out several groups of small-scale model tests to discuss the influence of longitudinal inclination angles on the active stability of tunnel faces in dense sand. Lei et al. [58] prepared a transparent clay with properties akin to those of *in situ* clay to investigate the active instability of shield tunneling faces. Zhang et al. [57] performed small-scale mode tests to determine the effect of blot-reinforcing tunnel faces. Ma et al. [59] used an optical laser and a charge coupled device high-speed camera to track the failure of tunnel faces in small-scale model tests.

In studies with various 1–g small-scale model tests, previous research has focused mainly on the active failure mechanism of tunnel faces. The study of the passive failure of tunnel faces has rarely been considered, including in laboratory small-scale model tests. This is because the traditional model tests mostly adopted methods that consider backward movement of rigid plate to model the active failure of tunnel faces. Wong et al. [10] and Qi [15] used methods involving the forward movement of rigid plate to simulate the passive failure of deeply buried tunnel faces based on centrifuge model tests. They obtained results in the passive ultimate support pressure and passive failure modes. Nevertheless, this type of experimental device also has limitations for simulating the passive failure of tunnel faces, such as an insufficient forward distance, inadequate thrust, and an uneven deformation of rigid plates. Although the test equipment for active failure simulation has been upgraded [60,61], it may still be inappropriate for exploring the passive stability of tunnel faces. Moreover, the lack of test data frustrates the analysis of the passive stability of shallow shield tunnel faces in coastal backfill sand. In contrast to the more intensively studied active failure of the face, passive failure has yet to be discussed in detail, despite its being easily induced at shallow burial depths in backfilled sand strata. Therefore, understanding the passive failure features of tunnel faces and selecting an appropriate method to deduce the support pressure of tunnel faces through small-scale model tests is of practical interest to engineers responsible for shallow shield tunnel engineering works in coastal backfill sand.

In this study, an improved experimental apparatus was designed to model the passive failure of tunnel faces at shallow burial depths in coastal backfill sand strata, using four sets of 1–g model tests. Failure mode and velocity field distribution were compared based on the experimental and numerical results. The details of experimental studies, including the experimental instruments, materials, and procedures, are described in Section 2. The analysis of support pressure, failure process, and failure mode of tunnel faces is presented in Section 3. In Section 4, a series of numerical simulations, to determine the distribution of velocity fields in the failure zone, are reported.

2 1–g small-scale model test

2.1 Details of model test system

The schematic sketch of model tests is shown in Fig. 2. The experimental system includes a model tunnel, a model container, data measuring apparatus, and image-capturing equipment; the model container was used to hold the soil, and the model tunnel simulated the shield tunneling. The apparatus, consisting of the earth pressure cell, a displacement sensor, a sensor data acquisition device, and a computer, was used to determine and display the support pressure value. The image-capturing equipment, including a digital camera and spotlights, served to record the displacement of the soil at its faces.

As shown in Fig. 3, the tests were implemented in a container measuring 700 mm × 500 mm × 700 mm (length × width × height). The outer frame of the model container was made of steel bars; the bottom plate and rear wall were fabricated from a 10-mm thick steel plate; all the other side walls were fabricated from a 10-mm thick transparent acrylic panel through which the tested soil could be viewed throughout the test. The symmetry principle was applied to help observe the failure process of tunnel faces more visually. Thus, the model tunnel was axially split into a semi-circular cross-section, and the vertical symmetric plane was then directly observed through the side wall [62]. Details the model test system are shown in Fig. 3. A semi-circular hole with a radius of 90 mm was cut into the rear wall, some 170 mm from the bottom plate. The tunnel model, made of a 10 mm thick half-cylinder steel plate, was installed in this opening. The inner diameter of the model tunnel was 150 mm; the tunnel model protruded 150 mm into the model container.

In past model tests, the forward movement of the rigid plate was often used to simulate the passive instability of tunnel faces; however, this traditional method allowed sand to leak between the tunnel model and the rigid plate, and insufficient forward movement led to the incomplete passive failure. A polyoxymethylene (POM) semi-circular piston with a thickness of 100 mm was designed. This piston was installed in the tunnel model such as to avoid leakage of the sand and ensure adequate forward

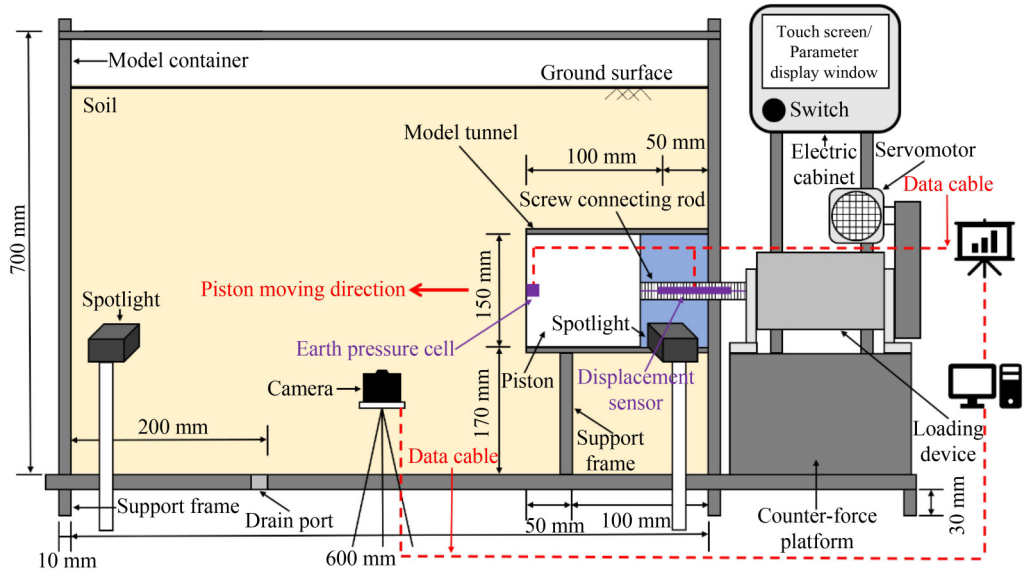

Fig. 2 Schematic representation of the experimental system.

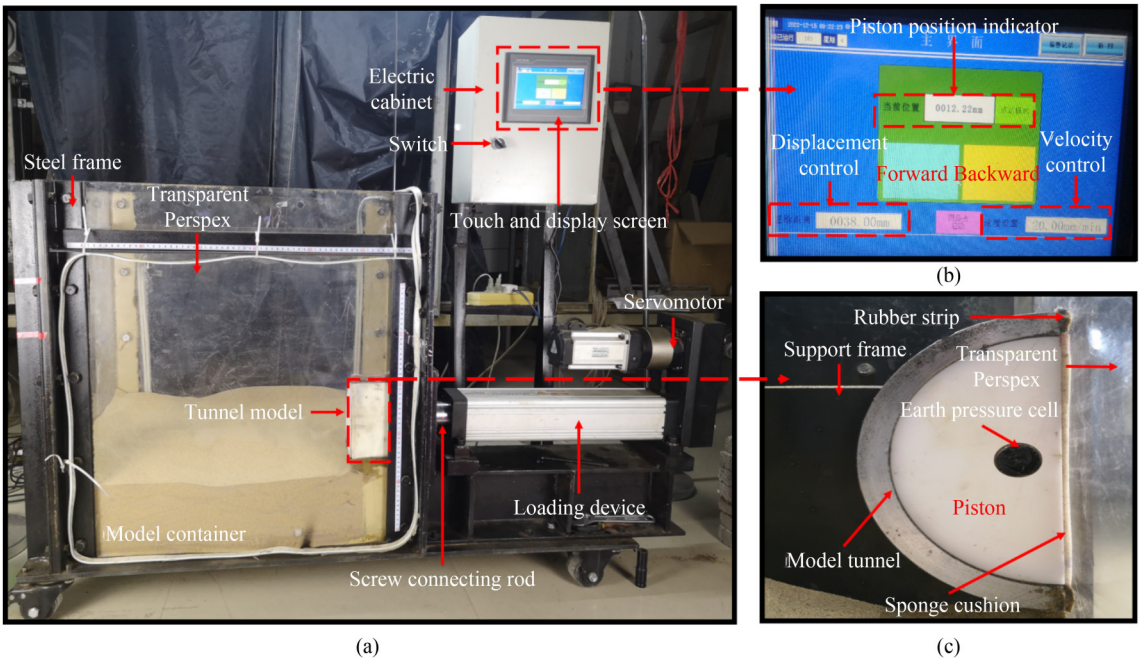

Fig. 3 Model test instrument: (a) model container; (b) touch-screen panel; (c) model tunnel (end view, without sand in the model container.

motion. The piston diameter was 150 mm, slightly smaller than that of the semi-cylindrical tunnel model. Moreover, POM has excellent mechanical and self-lubricating properties and is frequently used to manufacture gears and bearings. This material ensured that the piston was not easily deformed and prevented the piston from generating excessive friction with the model tunnel shell and the acrylic panel. The piston was fixed to a screw connecting rod, and a loading device was installed on one end. The back-and-forth movement of the piston was controlled by an external servo-motor. The motor thrust was crucial during the test, and the loading device could provide a maximum thrust of 1500 kN. The distance moved and speed of the piston were controlled by the operator, using a touch-screen control panel, and the maximum piston movement was 100 mm. As shown in Fig. 3(b), the touch-screen control panel not only allowed control of the piston movement but also displayed movement parameters (displacement and velocity). Accurate and automatic control of the piston movement was the main function of the control panel. On the one hand, the touch-screen control panel was used to

set the displacement and velocity of the piston. On the other hand, the touch-screen console could also display the movement parameter and the piston location. For example, as shown in Fig. 3, we first entered specific values for displacement and for velocity, then clicked the forward and backward buttons; lastly, the piston moved according to the default movement parameters.

It was essential to impede sand from penetrating the gap between the semi-circular piston and the side wall of the model container. Consequently, the boundary between the half-cylinder and the acrylic panel was lined with a 1 mm thick sponge cushion (Fig. 3(c)). To prevent leakage through the gap between the piston and lateral wall, a spongy cushion with a thickness of 2 mm was attached to the side of the piston. Tognon et al. [63] noted that it is necessary to implement frictional treatment for laboratory tests, especially for small-scale tests. This test used petroleum jelly to reduce friction between the sidewall and the sand. Meanwhile, petroleum jelly was smeared against the surface of the spongy cushion to reduce friction and further enhance the seal around the piston. A micro-earth-pressure cell was installed on the piston to measure the face support pressure at the piston. The displacement of the piston was measured using the displacement sensors mounted on the screw connecting rod. The sensors and data acquisition device fabricated by XACGQ, a Chinese sensor manufacturer, were adopted to monitor the pressure and displacement during tests. The normal measurement ranges of pressure cells and displacement sensors were from 0 to 100 kPa and 0 to 100 mm, respectively. The piston could be extended into the model container to induce tunnel face blow-out: details of the movement of the piston during the test will be described in Subsection 2.3.

2.2 Experimental soil preparation

The model experiments were conducted using dry sand in order to easily identify variations in the failure mode. To minimize the effect of grain sizes on soil-structure interaction, as considered by Ref. [51], the relationship between the grain size of the test soil and the tunnel diameter should satisfy the following condition:

$$\frac{D}{d_{50}} > 175, \tag{1}$$

where D represents the tunnel diameter and d_{50} represents the average grain diameter of test sand.

The backfill sand was collected from Xiamen City in China. The sand was dried before the experiment, and grains larger than 2 mm in diameter were screened out using a 2 mm diameter sieve. The particle size distribution of the backfill sand is displayed in Fig. 4, from which it can be seen that d_{50} is equal to 0.2 mm. Consequently, the D/d_{50} value is 750, satisfying the requirement of

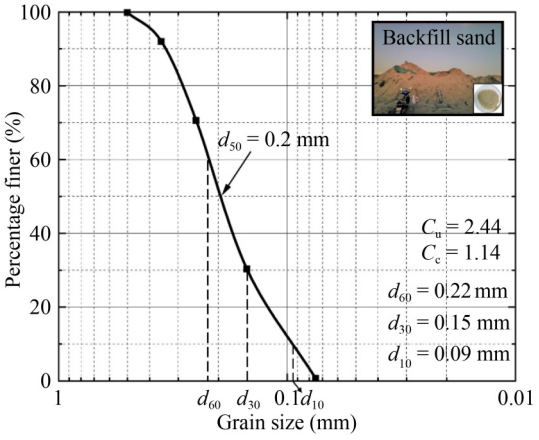

Fig. 4 Particle size distribution of the experimental sand.

Eq. (1). In addition, the sand relative density D_r value is 0.45, and the unit weight ρ value is 14.51 kN/m^3, implying a medium density sand.

The moisture content of the sand was determined by the oven-drying method, and the mechanical properties of the backfill sand were obtained from direct shear tests. Key material parameters are listed in Table 1. The final moisture content of the sand was approximately zero, so it could be considered dry sand. Thus, model tests were conducted using dry sand (dry granular material), allowing changes in the face support pressure and the evolutions of the failure pattern to be easily recorded. Dry sand was also considered in existing works [8,9,57]. Furthermore, Kirsch [51] discovered that apparent cohesion and dilation effects occurring with damp material might lead to erroneous experimental results. Moreover, the relative density of test sand should be controlled to within 0.6 to weaken the impact of apparent cohesion and dilatancy as far as possible [56]. The dry pluviation method [51,56] was employed to prepare the backfill sand stratum in the model container. Following the summary provided by [56], the drop height of the sand was set to 60 mm. Using the solution provided by Ref. [51], the thickness of each sand layer was 50 mm. A 10-mm thick layer of slightly blue-dyed sand was laid between two adjacent layers of test sand in the model container, the better to capture soil deformation. After each layer of blue-dyed sand was added, the sand was tamped and flattened manually.

Table 1 Properties of the sand

Parameter	Value
unit weight, γ (kN/m^3)	14.51
relative density, D_r	0.45
internal friction angle, φ (°)	30.16
cohesion, c (kPa)	0
moisture content, w (%)	0.18
mean grain size, d_{50} (mm)	0.2

2.3 Test method and procedure

Based on the branch project of Xiamen Metro Line 3, the shield tunnel with the diameter D of 6.3 m was taken as the engineering background, and the predominant cover thicknesses C, as given in Fig. 1 are 3.2, 5, 6.3, and 8.2 m. According to technical code [64], shield tunnels with burial depth ratios $C/D < 1.5$ are defined as shallow buried tunnels. Combined with engineering practice to model the behavior of shallow buried tunnels, four different burial depth rations C/D were considered in these tests: 0.5, 0.8, 1, and 1.3. The displacement control method [7,9,51,52,57] was selected to identify the tunnel face instability in four groups of model tests. In past studies, pushing the piston forward has been an accepted method of simulating sand blow-out driven by tunnel faces [10,11]. The movement of the sand was calculated with PIV, which studied the flow behavior by locating the trajectory of tracer particles. Over the last few decades, this method has been widely utilized in face stability analysis because the displacement at the sand particle scale can be analyzed. The sand particle movement was tracked by analyzing photographs taken by the camera using the digital image correlation technique. Figure 5(a) shows the set-up of the image-capturing experiment with the camera and two spotlights. A series of tests were executed in a dark room. The camera was positioned on the side of the model container to photograph the deformed sand through the transparent acrylic panel. Two 50-W spotlights were arranged on both sides of the model container to supply continual lighting for the model container throughout the tests. Photographs were recorded with a Canon D1000 digital camera. The support pressure and displacement of the piston were continuously recorded throughout the test. The trajectories of sand particles were collected by post-processing the images with the PIV software. A captured image for the analysis in the test is shown in Fig. 5(b) when $C/D = 1$, where b and h represent the width and height of the analysis area.

Liu et al. [9] believed that the support pressure remained unaffected by changes in piston velocity when it was below a specific threshold. In tests, the piston was controlled by means of the control panel, and the piston speed was set to 10 mm/min. As illustrated in Fig. 3(b), the piston was pushed toward the sand by pressing the forward button on the touch screen. The speed and distance of the piston could be set through the touch screen. The test was terminated by switching off the servo-motor when the piston reached its maximum forward displacement of 60 mm. Digital photographs of the soil were recorded at 2-s intervals as the piston moved. The maximum distance setting is helpful for generating noticeable soil deformation due to the passive failure of tunnel faces.

3 Experimental results and analyses

3.1 Characteristics of failure mode

As discussed in Refs. [10,17], the soil ahead of tunnel faces was pushed toward the ground surface when the support pressure exceeded a threshold value, which caused ground uplift and blow-out. This failure mode of passive instability on tunnel faces can be clearly observed in our tests. Figure 6 illustrates the failure mode of tunnel faces at different burial depth ratios as the piston reached its maximum displacement. The intersection angle α between the displacement direction of sand particles and the direction of piston movement is shown in Fig. 6; α reflects the potential movement of the sand. The widths of the ground surface in the failure zone were approximately 291 mm, 305 mm, 312 mm, and 319 mm when C/D was 0.5, 0.8, 1, and 1.3, respectively (Fig. 6); failure angles were approximately 25°, 24°, 22°, and 20°, respectively (Fig. 6). Many visible zones of deformation (as suggested by movement of the blue-dyed sand) appeared on the sand surface in the model container. Chambon and Corté [48] obtained the failure mode by

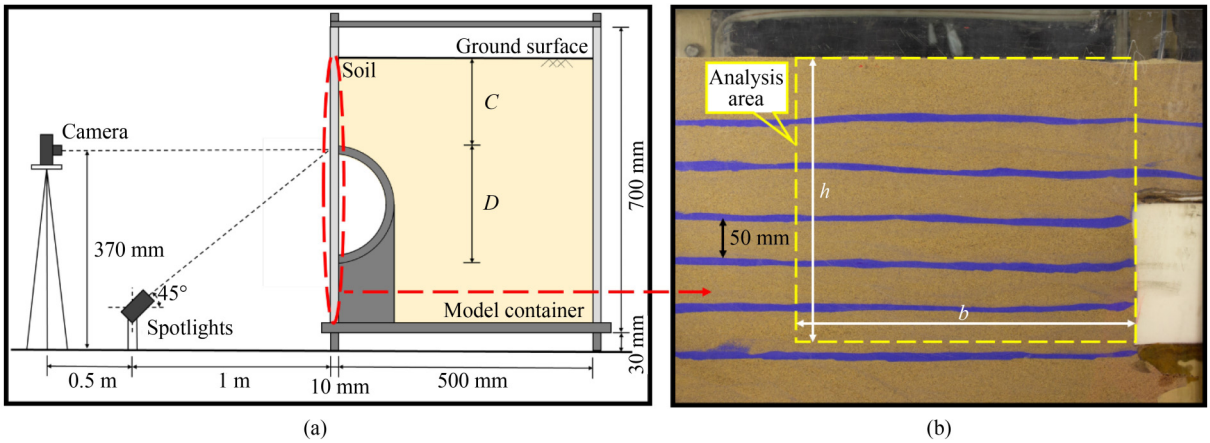

Fig. 5 Experimental apparatus: (a) transverse view; (b) analysis area of PIV at $C/D = 1$.

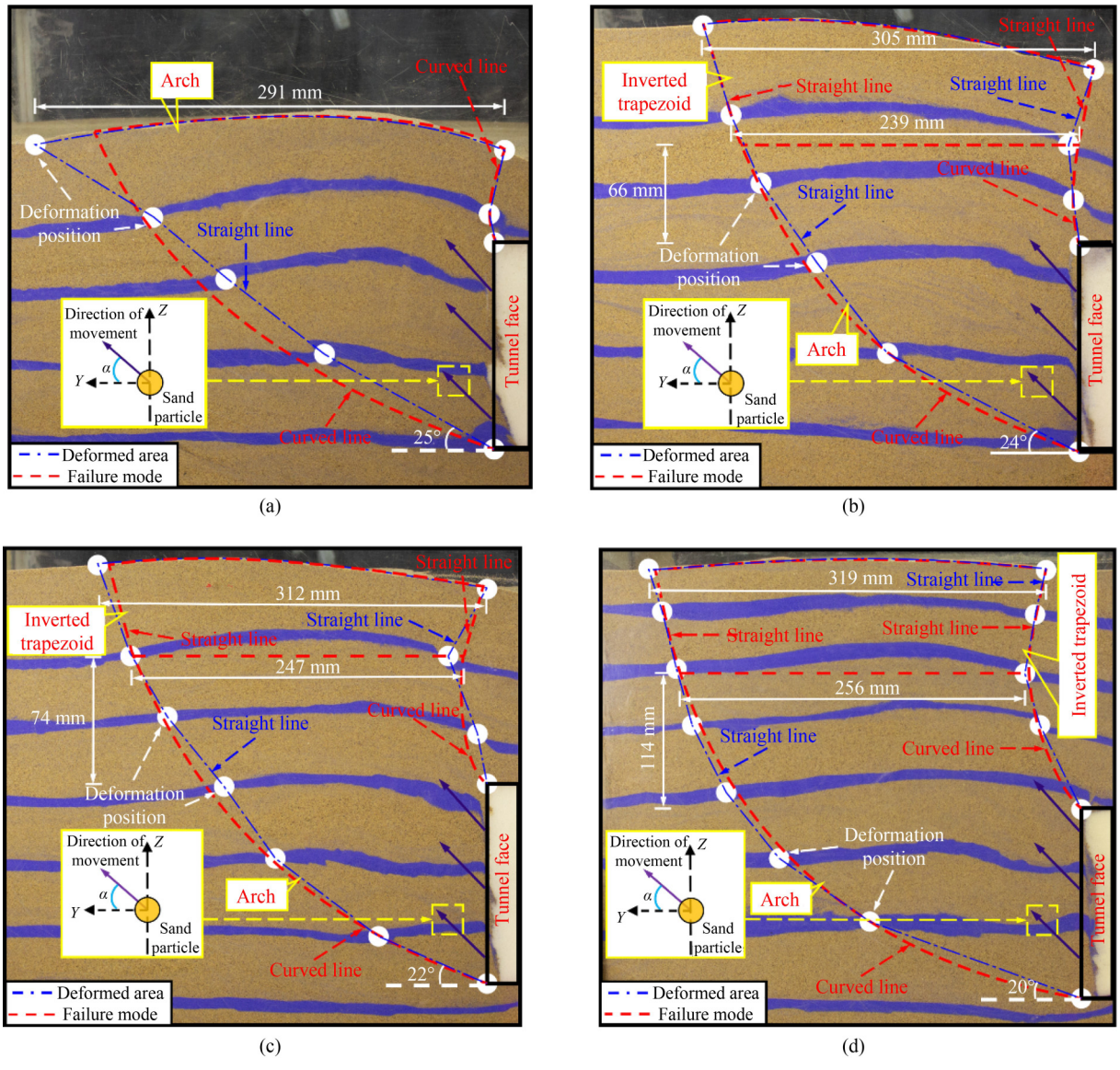

Fig. 6 Descriptions of failure mode at different burial depth ratios *C*/*D*: (a) 0.5; (b) 0.8; (c) 1; (d) 1.3.

carefully tracing the position of colored sand layers in the deformed soil based on centrifugal model tests. Many researchers [56,57,60] have used this method to determine failure modes in model tests. Thus, these loci of deformation of blue-dyed sand layers were connected by straight lines to map the extent of deformed areas. Based on these loci of limits of blue-dyed sand deformations, the failure mode was fitted by curved lines with reference to the guidance in Ref. [58]. The irregular straight lines outside the boundary of deformed areas could be approximated as a combination of straight and curved lines to identify the shape associated with each mode of failure. The shape of the failure mode could be regarded as an arch when C/D = 0.5, as observed in [10,33]. Two curved lines that consist of the arched failure mode could be represented by two logarithmic spirals [33,43]. The failure mode could be divided into two parts when C/D = 0.8, 1, or 1.3. The geometry of the one part ahead of tunnel faces was arcuate, similar to the failure mode at C/D = 0.5; the geometry of the other part near ground surfaces could be described as an inverted trapezoid similar to that found by Refs. [15,38]. A difference in failure modes between the case of C/D = 0.5 and those with C/D = 0.8, 1, and 1.3 emerged; the support pressure, failure process, and failure mode were examined to explain this difference, in order to comprehend the passive failure mechanism and gain evidence for developing the theoretical analysis model.

3.2 Support pressure of tunnel face

The earth pressure cell and displacement sensor on the piston (Fig. 3), provided data on the support pressure, p, and displacement, s, of tunnel faces. To minimize the effect of non-uniformity on support pressures and displacements, sensors were calibrated by the approach of

[51] before tests, as detailed in Appendix A. The changing pattern of the support pressure p of tunnel faces versus the face displacement s with four groups of burial depth ratios for C/D = 0.5, 0.8, 1, and 1.3 are presented in Fig. 7. The basic trends of the pressure-displacement (p–s) curves under different burial depth ratios were similar. The support pressure of tunnel faces increases with burial depth ratios. The support pressure rose abruptly to a maximum value, termed the ultimate support pressure p_u, at the face displacement of analogously 30–40 mm, and then gradually decreased to a stable value with the increase of the face displacement. The convex pressure-displacement curves in experiments were also found by other scholars [10].

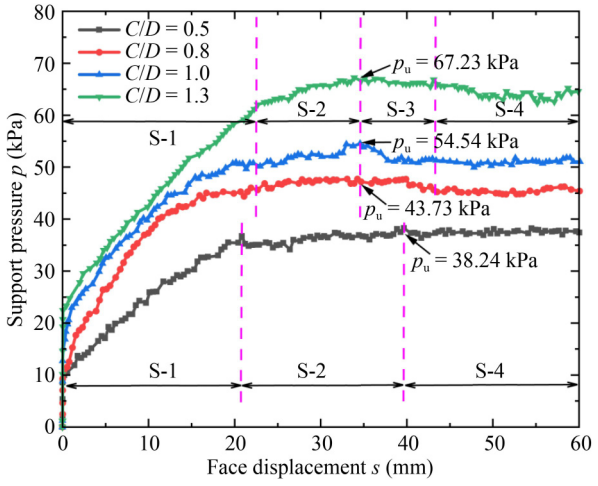

Fig. 7 Variations in the face support pressure p with face movement s.

Similarly, as presented in Fig. 7, the variation trend of the p–s curve was the same in the three cases of C/D = 0.8, 1, 1.3. The value of p rose to its maximum of 38.24 kPa when C/D = 0.5, as s increased to 40 mm; however, the support pressure p did not show a prominent increase but remained stable as s continued to increase. As shown in Fig. 7, the p–s curve with C/D = 0.5 could be divided into three stages. The primary difference between the curve with C/D = 0.5 and the other curves (C/D = 0.8, 1, and 1.3) occurred after the maximum value for p was exceeded during the rebound stage. As noted by [7,8,51,56,57], the peak shear strength of sand was fully mobilized after the maximum support pressure was reached, then the support pressure dropped, which was caused by strain-softening behaviors. The p–s curves were divided into four stages, shown by pink dashed lines and denoted by S-1, S-2, S-3, and S-4 in Fig. 7.

S-1 stage: a significant increase of p. The support pressure of tunnel faces sharply increased, triggered by the piston movement. During this period, the sand was subjected to its full the shear strength, and elastic shear deformation in the sand near the piston occurred.

S-2 stage: a slow increase of p. With the continuous increase of face displacement s, the support pressure p increased slowly until the maximum value p_u was achieved. The soil in front of the piston steadily evolved toward limit states, and plastic deformation appeared.

S-3 stage: a slight decrease of p. As the face displacement s continuously increased, the support pressure p decreased slowly after reaching the ultimate support pressure p_u. The instability zone of the sand near the piston increasingly extended to the ground surface in this process.

S-4 stage: a stable stage of p. The support pressure p did not appear to increase but fluctuated within a small range. During this period, a blow-out occurred at the tunnel face, uplifting the ground surface.

The definition of different stages differs to some extent between what is the case for $C/D \neq 0.5$ and for C/D = 0.5. The slope of curves in stages S-2 and S-3 increases when $C/D \neq 0.5$; the support pressure p did not noticeably decrease after stage S-2 when C/D = 0.5, and the value p gradually stabilized. The instability of the tunnel face was more easily triggered where $C/D \leqslant 0.5$. Besides, the maximum support pressure and the following decrease when C/D = 1.3 were greater than in other cases (C/D = 0.5, 0.8, and 1). This suggests that an appropriate burial depth ratio can improve the stability of tunnel faces of shallow shield tunnels. Since previous works [10,11,15,61] deemed the ground surface to be an unconstrained boundary, the stress in the sand near the ground surface was released when the passive failure of tunnel faces led to the uplift. The strain-softening of the sand has nothing like enough time to occur when C/D = 0.5, and the stress relief on the ground surface was extremely rapid, thus hindering any decrease of pressure. The ultimate support pressure progressively decreased to stable values when C/D = 0.8, 1, and 1.3, a behavior that might be attributable to the strain-softening of the sand and the stress relief on the ground surface. However, this decrease value is less marked, and these percentage decreases are 7.8%, 8.3%, and 10.75% when C/D = 0.8, 1, and 1.3. This implied that the increase in burial depth ratios dramatically delayed the stress relief on the ground surface and fully mobilized the strain-softening of the sand. Therefore, the rebound phenomenon might be caused by the strain-softening in the sand and the stress release on the ground surface.

3.3 Failure process and failure zone

The variations of displacement fields (Fig. 8) and shear dissipations (Fig. 9) of sand in front of tunnel faces were explored to evaluate the failure process and failure zone of tunnel faces. The contoured displacement fields in Fig. 8 could be used to demarcate the failure zone. The shear band could be identified in Fig. 9 by the area of

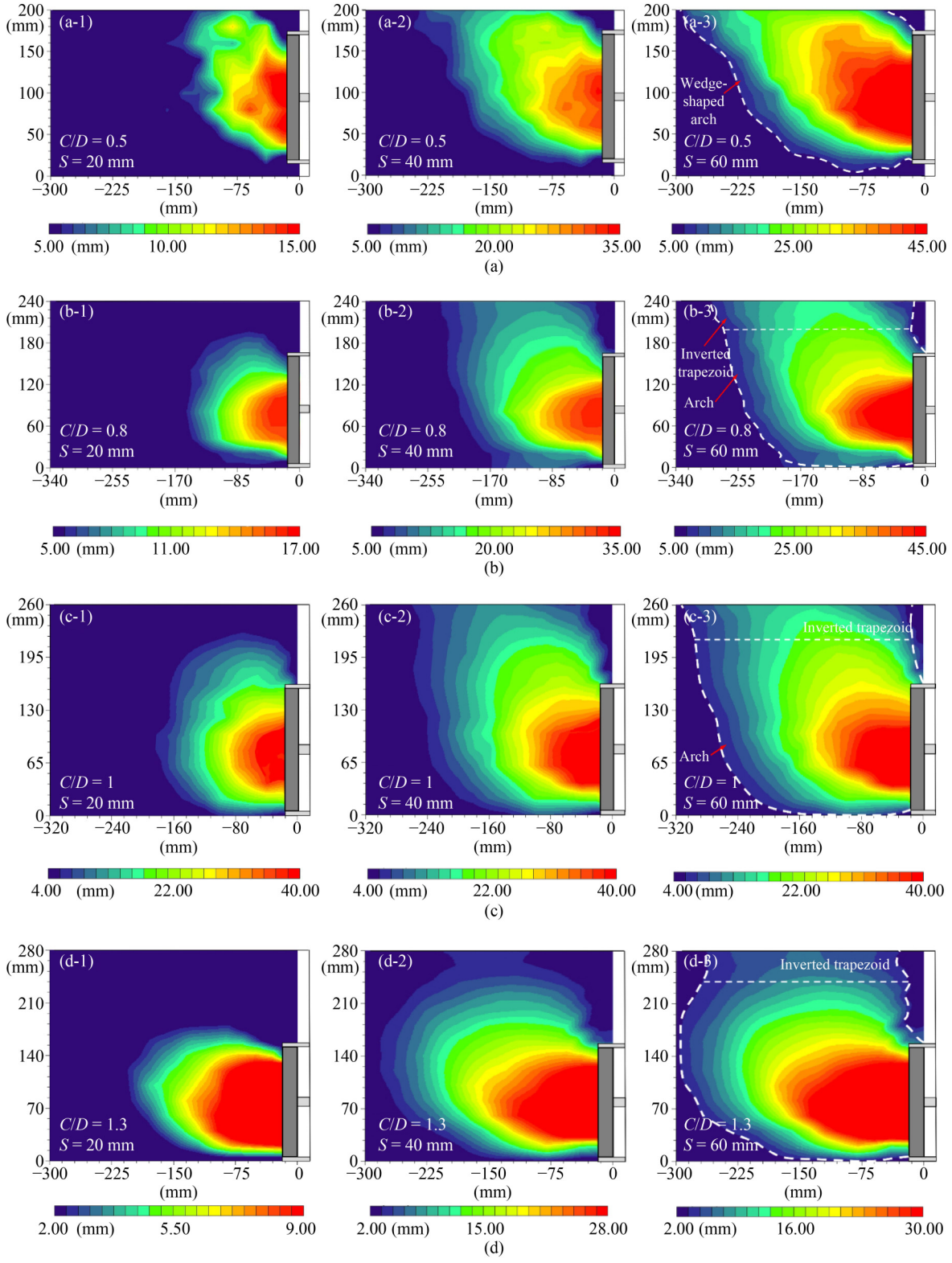

Fig. 8 Displacement fields of soil for different burial depth ratios C/D: (a) 0.5; (b) 0.8; (c) 1; (d) 1.3.

shear-strain concentration. A series of representative displacement fields and shear bands were selected, where face displacements of s = 20, 40, and 60 mm represent three stages in the p–s curve with C/D = 0.5, respectively; face displacements of s = 20, 40, and 60 mm represent the increase stage, the decrease stage, and the stable stage in p–s curves in three cases of C/D = 0.8, 1, and 1.3, respectively.

The displacement field of sand during testing is shown in Fig. 8. The size of failure zones in front of tunnel faces

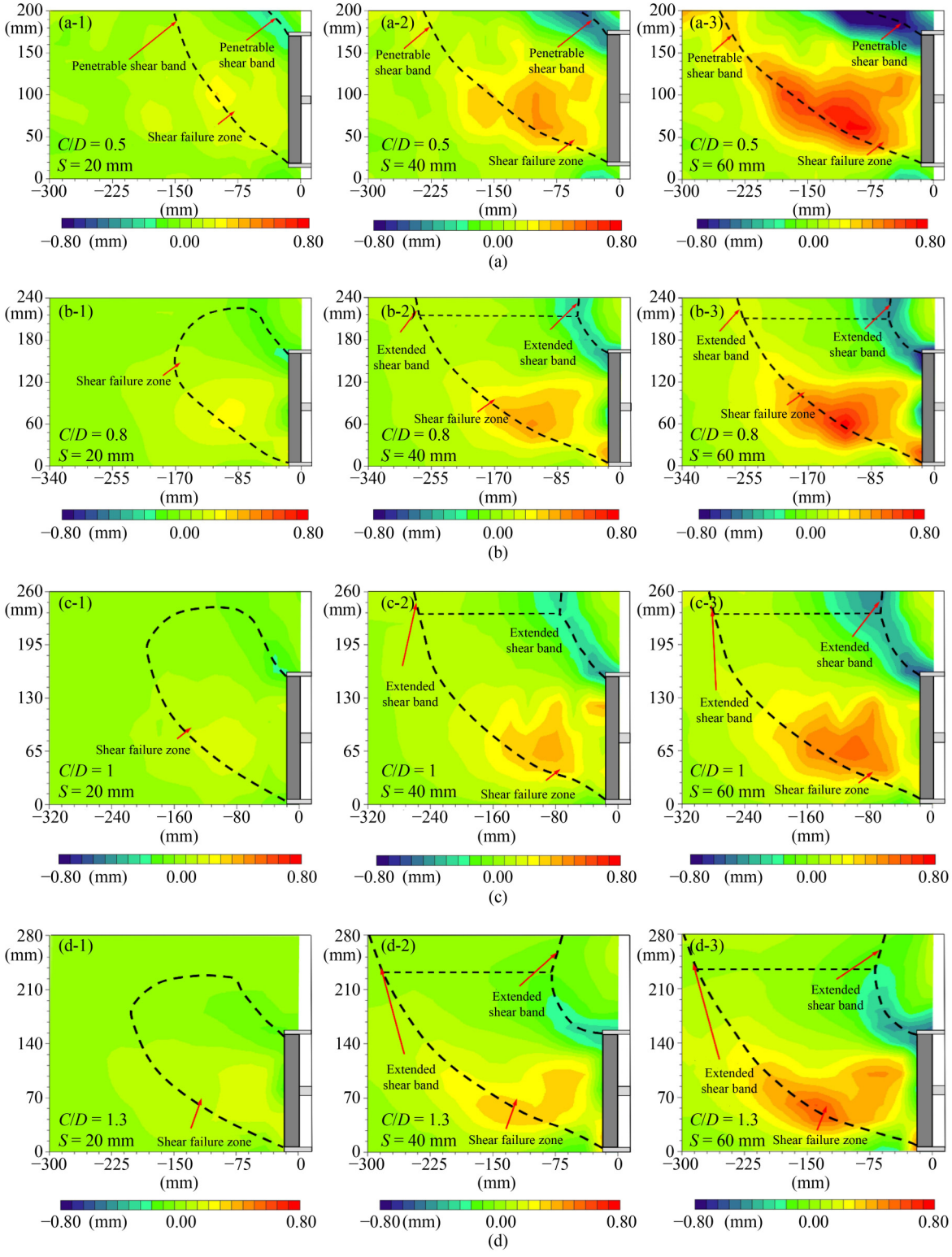

Fig. 9 Shear strains of soil for different burial depth ratios C/D: (a) 0.5; (b) 0.8; (c) 1; (d) 1.3.

differs in each case. In the extremely shallow case (i.e., C/D = 0.5), the failure zone was formed ahead of tunnel faces when s = 20 mm, initiating from the invert and crown of tunnels in a curved direction toward the ground surface. At this moment, the failure zone was outcropping. With the increase of s, failure zones at different stages of the p–s curve have outcropped. During this process, the support pressure reached its peak value, indicating the attainment of peak shear strength of the soil, and the sand ahead of tunnel faces entered a limited state. Finally, the outcropping length of failure zones was essentially constant when s = 60 mm; the failure zone

consisted of two curved lines. This showed that the sand in front of tunnel faces had been completely destabilized and that the geometric failure zone no longer changed. Consequently, the failure zone when C/D = 0.5 was defined as an outcropping failure zone with a wedge-shaped arch pattern.

In the appropriately shallow cases (i.e., C/D = 0.8, 1, and 1.3), as shown in Fig. 8, the evolution and shape of failure zones were different from those in extremely shallow cases, where the former covered a larger extent with a more complicated boundary. The failure zone did not reach the ground surface in the initial stage (i.e., s = 20 mm), and the contour of failure zones ahead of the tunnel face emerged as an arch. With increasing s, the failure zone extended toward the ground surface; the contour of failure zones above the tunnel changed from an arch to an inverted trapezoid. Combining information shown in Figs. 7 and 8, it can be seen that the failure zone extended to the ground surface when the support pressure reached its maximum value. As a result, when C/D = 0.8, 1, and 1.3, the inverted trapezoid failure zone near the ground surface was defined as the extended failure zone. Especially in the case of C/D = 1.3, the sand at tunnel faces reflected better stability, and the extended failure zone was not apparent. Accordingly, the configuration of failure zones for appropriate shallow burial cases (i.e., C/D = 0.8, 1, and 1.3) was of an inverted trapezoidal-arch-type, indicating that the improved theoretical model [38] could be applied to the passive stability analysis of tunnel faces. Besides, the extended failure zone (i.e., occurring at C/D = 0.8, 1, and 1.3) differed significantly from the outcropping failure zone (i.e., C/D = 0.5): the shear failure of the sand mainly occurred in front of the tunnel face. The outcropping failure zone might suggest that the sand on the ground surface was also subject to emergent shear failure, but the sand in the extended failure zone might not generate shear failure. This assumption will be verified in the subsequent analysis of shear bands.

The shear strains in the sand for different cases are illustrated in Fig. 9. The shear band could be identified by the centralized area of the shear strain [47,51,56,57,60]. As shown in Fig. 9, the concentration of shear strains became more pronounced as the face moved, and two significant shear bands were found. Lower and upper shear bands originated from the invert and crown of tunnels. In the initial stage (i.e., s = 20 mm), when C/D = 0.5, lower and upper shear bands reached the ground surface. With the increase of face displacement s, two shear bands consistently penetrated the ground surface, revealing that the shear failure of sand in front of tunnel faces invariably outcropped when C/D = 0.5. The development of shear dissipations was similar for C/D = 0.8, 1, and 1.3, as displayed in Fig. 9, but different from the case of C/D = 0.5. Two noticeable shear bands in front of tunnel faces could be attributed to the shear failure of the sand. Lower and upper shear bands originated from the tunnel invert and the tunnel crown, respectively; these shear bands spread to a certain height above the tunnel crown and extended to the ground surface. Two shear bands became less pronounced near the ground surface because of the extension of the shear bands. Shear failure mainly occurred ahead of tunnel faces in all cases. In contrast, the shear failure did not always appear near the ground surface when the burial depth ratio C/D was 0.8, 1, and 1.3, respectively.

As illustrated in Fig. 9, when s = 60 mm, two significant shear bands had been fully formed under all four cases, and two shear bands defined the boundary of failure zones. In addition to the two significant shear bands, a less distinct sub-shear band was also discovered. Moreover, a similar situation—shear-band bifurcation—had been discovered in past research [9,51,57]. This implied that the passive failure of tunnel faces was primarily generated by shear failure, and the size of the failure zone was enlarged as the burial depth ratio increased. When C/D = 0.5, this shear failure propagated to the ground surface, resulting in outcropping shear bands. However, the shear failure in front of tunnel faces did not wholly propagate to the ground surface for C/D = 0.8, 1, and 1.3. Shear bands near the ground surface had visibly extended. It might be caused by stress release from the soil near the ground surface, driven by the upward thrust of the sheared sand mass. Since the ground surface could be regarded as an unconstrained boundary, the sand near the ground surface did not generate shear failure in appropriately shallow tunnels (i.e., C/D = 0.8, 1, and 1.3). At this stage, the stress in the sand near the ground surface was first released to induce ground surface uplift and extended shear bands. Hence, when C/D = 0.8, 1, and 1.3, the failure zone ahead of tunnel faces caused by shear failures was called the lower failure zone, and the failure zone near ground surfaces formed by extended shear bands was called the upper failure zone. However, the lower failure zone existed only in the case of C/D = 0.5. In conclusion, the shapes of the lower and upper failure zones were an arch and an inverted trapezoid, respectively, which coincided with the contour of failure modes and displacement fields. Likewise, the shear bands in lower and upper failure zones could be matched by two curved and two straight lines. Therefore, the variation of shear strains was aligned with the boundary of failure modes as seen in Fig. 6 and the development of displacement fields as seen in Fig. 8, signifying that the failure mode could be judged based on the distribution of shear bands. Furthermore, the pattern of upper failure zones in the surrounding sand observed from these experiments was akin to the feature in other investigations [10,15].

3.4 Mechanisms of passive failure formation

According to the results described in Subsections 3.1 to 3.3, the face support pressure and sand displacement distributions were related to the failure mode. A series of model tests under shallowly buried conditions was also carried out for further elaboration, and test results of failure modes are present in Appendix B. Based on data furnished by different model tests [51,55,65], the failure mode could be determined by the boundary of failure zones with different geometries. The combination of two logarithmic spirals, as presented by Refs. [31,33], described the passive failure mode for exceptionally shallow tunnels (i.e., $C/D \leqslant 0.5$). As shown in Fig. 10, the failure mode for appropriately shallow tunnels (i.e., $C/D > 0.5$) could be divided into lower and upper failure zones, the lower failure zone was bounded by two logarithmic spirals, and the upper failure zone was bounded by two straight lines. Additionally, the geometrical parameters h, l, and L, as shown in Fig. 10, are proposed to depict the failure modes in the appropriately shallow tunnels (i.e., $C/D > 0.5$), where h represents the height from the top of the failure zone to the tunnel crown; l represents the width of the failure zone; and L represent the width of the failure zone on the ground surface. The mechanism of passive failure formation was revealed through the sand particle displacements.

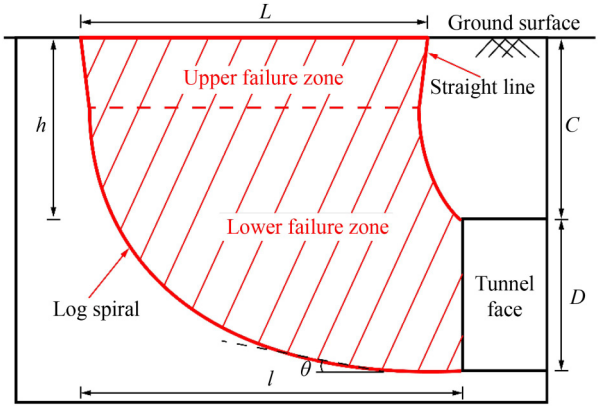

Fig. 10 Geometries of the passive failure mode for $C/D > 0.5$.

The movement of sand particles in the passive failure of tunnel faces is illustrated in Fig. 11. During shield tunneling, as the tunnel face moved forward, sand particles in front of tunnel faces were compacted to form a soil arch. These sand particles moved upward with the development of soil arches, and the stress on the ground surface was released. In the extremely shallow cases (i.e., $C/D = 0.5$), the soil arch reached the ground surface when shear failure was outcropped, leading to a huge uplift on the ground surface. As shown in Fig. 8, the magnitude of sand displacements in failure zones varied at different elevations, with those at the top being significantly lower than those at the bottom, notably for the zone near the ground surface. It demonstrated that the effect of soil arches gradually decreased as the burial depth ratio increased. Although the soil arch for appropriately buried cases (i.e., $C/D = 0.8$, 1, and 1.3) could propagate to the ground surface, its effect was significantly diminished. In addition, the sand stress at the tunnel crown was released earlier than that at the tunnel invert; as shown in Fig. 9, the shear failure band at the tunnel crown first reached the ground surface. It can be concluded that a self-stabilized region was developed at a certain height above such tunnels as the burial depth ratio increased, which prevented the shear failure from extending further. By this time, the upper failure zone was extended since the relief of sand stress on the ground surface. Diverse effects of stress relief on the ground surface lead to variations in the dimensions of the upper failure zones under different burial depth ratios.

4 Discussions

4.1 Comparison and verification

The movement behaviors of the soil ahead of tunnel faces were studied using numerical simulations, for comparison with the experimental findings. Finite element analysis software Abaqus was applied to reveal the passive failure mechanism. Several 3-d finite element models with four groups of burial depth ratios (i.e., $C/D = 0.5$, 0.8, 1, and

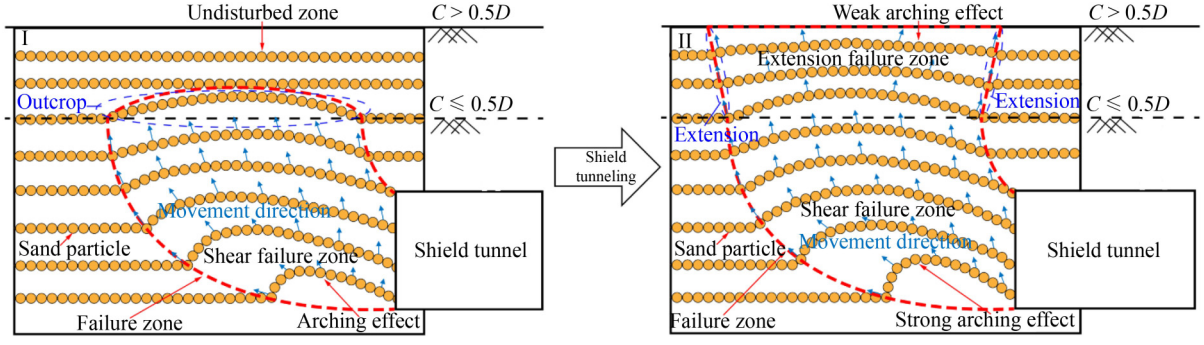

Fig. 11 Schematic representation of passive failure particle displacements around tunnel faces.

1.3) were created. The sand was characterized as an elasto-plastic material obeying the Mohr−Coulomb failure criterion. The elastic modulus and Poisson's ratio of the sand were 20 MPa and 0.35, respectively. Other parameters of the sand were derived from Table 1, and the surcharge load was set to zero. The lining of shield tunnels was assumed to be a linear elastic material with a Poisson's ratio, elasticity modulus, and thickness of 0.17, 33.5 GPa, and 0.01 m, respectively.

As shown in Fig. 12(a), only half of the model was built (exploiting symmetry). The length, width, and height of numerical models are 4D, 2.5D, and C + 2.5D, respectively, where C is the burial depth and D is the tunnel diameter. The boundary conditions of numerical models were considered as follows: all directions of displacements at the bottom of boundaries were fixed; the ground surface at the top of models was set free; the vertical boundaries at the sides of models were constrained by normal displacements. The sand and lining were modeled with C3D8R elements, and the whole model was meshed by 10435 elements and 12086 nodes.

The displacement control method was employed in model tests, so in order to reproduce the experimental conditions the displacement boundary was used to simulate the failure process. Meanwhile, a single-step excavation scheme was applied to simplify analyses [66]. First, the sand in the tunnel was excavated, and the shell was activated after the crustal stress of numerical models had been balanced. Second, the displacement boundary of tunnel faces along the Y-axis was made by controlling the forward velocity of each node on the tunnel face. Third, tunnel face blow-out could be triggered by progressively increasing the face displacement, during which the earth pressure at the face center was measured. Finally, the relationship between the support pressure and the center of face displacements could be described. When the support pressure reached a threshold value, the face displacement increased significantly, and the support pressure at this point was defined as the ultimate support pressure.

The change pattern of the support pressure, p, versus the face displacement, s, was derived from numerical results, as illustrated in Fig. 12(b). The trends in the numerical results were comparable to those determined experimentally (Fig. 7), except that no distinct decrease phenomenon was observed. The primary reason is that the strain-softening properties of the sand were not considered in the numerical simulations. Figure 12(b) indicates that as the burial depth ratios increase from 0.5 to 1.3, the ultimate support pressure p increases by approximately 48%, from 40.88 to 78.62 kPa. Moreover, the curves became steeper with an increasing burial depth ratio in the ascending stage of p–s curves, indicating that adopting an appropriate burial depth improved the stability of tunnel faces. As expected, the ultimate support pressure increased with an increase in burial depth ratios. These conclusions align with those of the experimental results (Subsection 3.2).

As plotted in Fig. 13, the ultimate support pressure p_u obtained from the present study was compared with the results derived from different works. In Fig. 13, the p_u value obtained from model tests was marginally lower than those obtained from numerical simulations, but these two results were the closest. Despite significant differences between the test results and the results of another three studies [31,33,38], the variations therein were similar. In particular, the trend of test results was consistent with the result of [38] because the influence of dilation angles was introduced by Ref. [38]. However, in all cases, the ultimate support pressure was overestimated due to the 2D mechanism of the upper bound analysis being considered by [38]. The ultimate support pressure might be underestimated by theoretical analyses [31,33] when C/D = 0.5; the ultimate support pressure might be overestimated when C/D > 0.5, perhaps because the dilatancy of the sand affected the boundary of failure

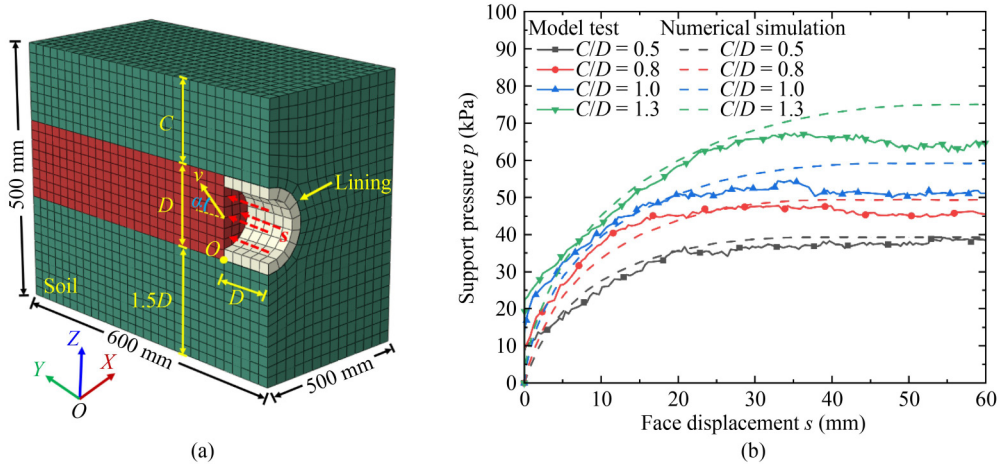

Fig. 12 Numerical result: (a) modeling strategy; (b) support pressure versus face displacement.

zones in small-scale model tests. Friction was unavoidable during the model test, which led to discrepancies between the practical parameters and those measured during testing. Consequently, considering the testing and calculation errors, the experimental and numerical results were highly similar, indicating that we successfully developed a valid geotechnical experimental system. The piston with sufficient travel and the solid and lubricant materials used in the experimental apparatus were more likely to induce passive failure of the face. The equipment will be further optimized to simulate face failure in future studies. An additional conclusion arising from Fig. 13 is that the discrepancy between theoretical solutions for appropriately shallow and extremely shallow burial conditions was considerable. There appears to be a critical threshold of burial depth ratios, beyond which the failure mechanism is significantly changed.

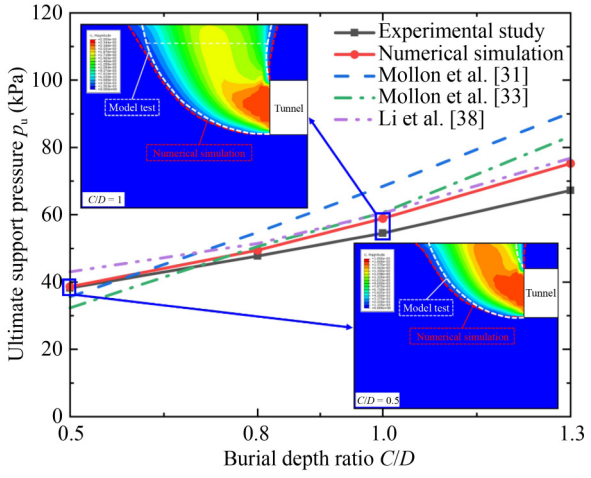

Fig. 13 Comparisons of ultimate support pressure p_u obtained by different studies.

Failure zones for two typical burial depth ratios (i.e., C/D = 0.5 and 1) are compared in Fig. 13. The extents of failure zones in these two typical cases that were determined through numerical simulation were found to be greater than those measured by the model test. The reason for this is that the failure zone cannot be determined intuitively from the results of numerical simulations. Instead, the displacement concentrated region can be deemed equivalent to the failure zone. It is noteworthy that the boundaries of the failed zones obtained by numerical models were comparable to those measured experimentally. In the appropriately shallow burial case, the configuration of failure patterns achieved by numerical simulations was also an inverted trapezoidal-arch-type mechanism. Specifically, the sand displacement near the ground surface gradually spread to both sides as the failure evolved when C/D = 1. The displacement field extended to near the ground surface, resulting from the stress relief and load transfer during tunneling. These conclusions align with those derived from experimental results in Subsection 3.3. Additionally, a series of geometrical parameters (h/C, l/D, and L/D) of the failure zone were compared in different studies when C/D = 1, as listed in Table 2. As found in Refs. [12,51], the active failure mode of tunnel faces was not outcropped when h/C < 1; in contrast, the active failure mode was outcropped when the value of h/C approached 1. In addition, the values of l/D calculated by Refs. [12,51] were 0.46 and 0.26, respectively; the values of θ calculated by Refs. [12,51] were 65° and 76°, respectively. As shown in Table 2, the parameter h/C calculated by different methods were all 1 when C/D = 1, which meant that passive failure modes of tunnel faces were invariably outcropped. The high value of l/D and the low value of θ implied that the failure mode of the passive instability was larger than those of the active instability. Eventually, the comparison results implied that the scope of passive failure modes was overestimated by these theoretical results [31,33,38], as illustrated in Table 2; the failure modes obtained from experimental and numerical results in this study were approximately close to the failure modes proposed by Refs. [31,33,38].

Table 2 Features of passive failure modes in different studies

C/D = 1	Ref. [31]	Ref. [33]	Ref. [38]	Model test	Numerical simulation
h/C	1	1	1	1	1
L/D	0.97	2.26	2.08	1.74	1.88
l/D	2.53	1.47	1.98	2.02	2.12
θ (°)	27	18	18	22	19

4.2 Effect of passive failure of the face on the sand stresses

Three stress ratios were specified to explore the stress release on the ground surface due to the passive failure of tunnel faces. The stress ratios in the X, Y, and Z-axis are $\lambda_x = \sigma_x/\sigma_{x0}$, $\lambda_y = \sigma_y/\sigma_{y0}$, and $\lambda_z = \sigma_z/\sigma_{z0}$, respectively, where σ_x, σ_y, and σ_z denote the earth pressure of ultimate states in the X, Y, and Z-axis, respectively; σ_{x0}, σ_{y0}, and σ_{z0} denote initial earth pressures in the X, Y, and Z-axis, respectively. In Fig. 12, the X, Y, and Z-axis denote the transverse, longitudinal, and perpendicular orientations, respectively.

Figure 14 gives stress ratios λ_x, λ_y, and λ_z of the perpendicular cross-sections along tunnels for two typical cases (i.e., C/D = 0.5 and C/D = 1). Red dots symbolized that the stress ratios in all directions were greater than 1 (i.e., $\lambda_x > 1$, $\lambda_y > 1$, and $\lambda_z > 1$), as illustrated in Fig. 14, and black dots signified that all stress ratios were less than 1 (i.e., $\lambda_x < 1$, $\lambda_y < 1$, and $\lambda_z < 1$). The stress ratios λ_x, λ_y, and λ_z within a specific range ahead of the tunnel face increased, which meant that shear failure was generated during tunneling. Moreover, the stress ratios λ_x, λ_y, and λ_z on the ground surface decreased, which implied

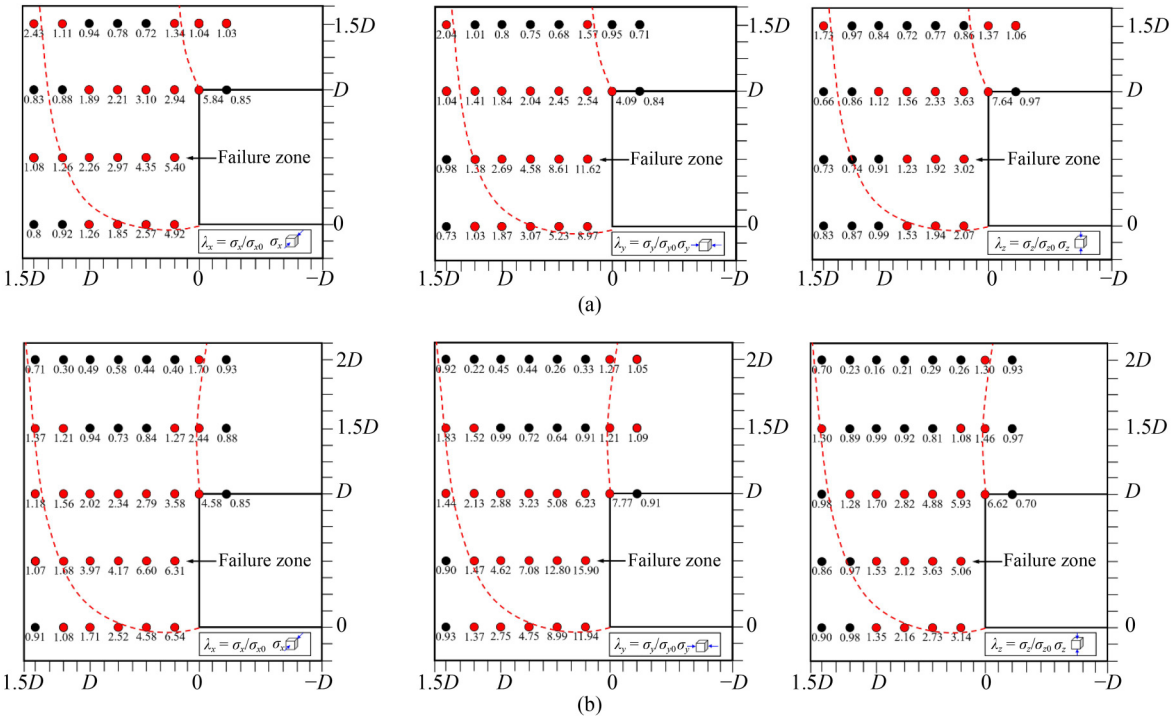

Fig. 14 Distribution of the stress ratios: (a) C/D = 0.5; (b) C/D = 1.

that stress relief had occurred. In conjunction with the previous section, the strain-softening of the sand was the essential reason for the rebound of p–s curves. Contrary to the case of active failure [7,57], the region of the sand with $\lambda_x > 1$, $\lambda_y > 1$, and $\lambda_z > 1$ could be regarded as the range of the failure zone, as shown by the red dots in Fig. 14. Specifically, stress ratios increased in front of tunnel faces and at the boundary of failure zones; in contrast, stress ratios decreased in other areas, especially in failure zones near the ground surface. This indicates that the relief of the sand stress near the ground surface occurs. As shown in Fig. 14, the distribution of black dots in failure zones was the inverted trapezoid when C/D = 1, and the distribution of black dots did not display a similar shape when C/D = 0.5. Additionally, the shear failure with C/D = 0.5 developed to the ground surface, but the shear failure with C/D = 1 did not. As shown in Fig. 14(b), stress ratios decreased within the horizontal range of 1.5D to 2.0D, indicating that a self-stabilizing region has formed at a certain height above the tunnels. The pushing action of the sand in shear failure zones led to the deformation of the sand in the self-stabilizing region. Ultimately, the results show that the stress relief of the sand at the ground surface prevents the expansion of shear failure zones and enlarges the failure zone near the ground surface, thereby verifying the analysis in Subsection 3.4.

4.3 Velocity distribution of failure zones

Determining the direction of sand movement is a limitation of model tests. To investigate the distribution of velocity fields, two typical cases with C/D = 0.5 and C/D = 1 were selected for analysis. Figures 15(a) and 15(b) show the distribution of velocity fields along the tunnel axis cross-section for C/D = 0.5 and C/D = 1. As shown in Fig. 15, when C/D = 0.5, the velocity direction on the ground surface was the same as that when C/D = 1, and the velocity field at the ground surface expanded significantly. This is because the stress near the ground surface decreased significantly due to the stress relief in the soil, resulting in the free movement of the soil in different directions. The numerical results of velocity direction were quantitatively investigated to explore velocity field distribution further. During the numerical simulation, the distributions of velocity vectors on the tunnel face and ground surface were collected and recorded. The movement characteristics of sand particles are revealed by the velocity inclination α (Figs. 9 and 12), where the crown of tunnel faces is taken as the origin.

Figure 16 illustrates the inclination of velocity fields at the tunnel face and at the ground surface, determined by the numerical simulation. The translational and rotational velocity fields established by Mollon et al. [31,33] relate to two commonly used failure modes in the stability analysis of tunnel faces. The difference between the two studies, Refs. [31,33], was the velocity direction and the shape of velocity fields in failure zones. On the one hand, the direction of soil movement was inclined in translational velocity fields and curved in rotational velocity fields. On the other hand, as depicted in Refs. [31,33], the translation and rotational velocity fields could be

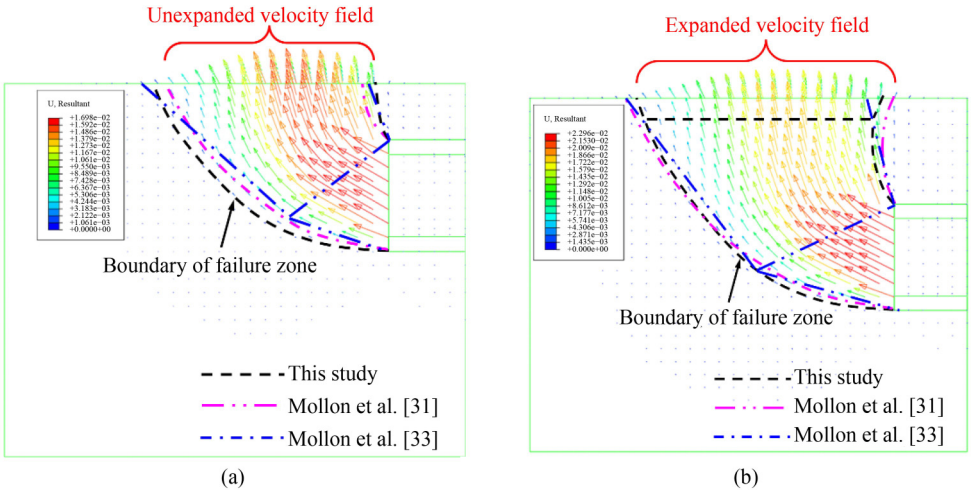

Fig. 15 Velocity field obtained by numerical simulations at s = 60mm: (a) C/D = 0.5, (b) C/D = 1.

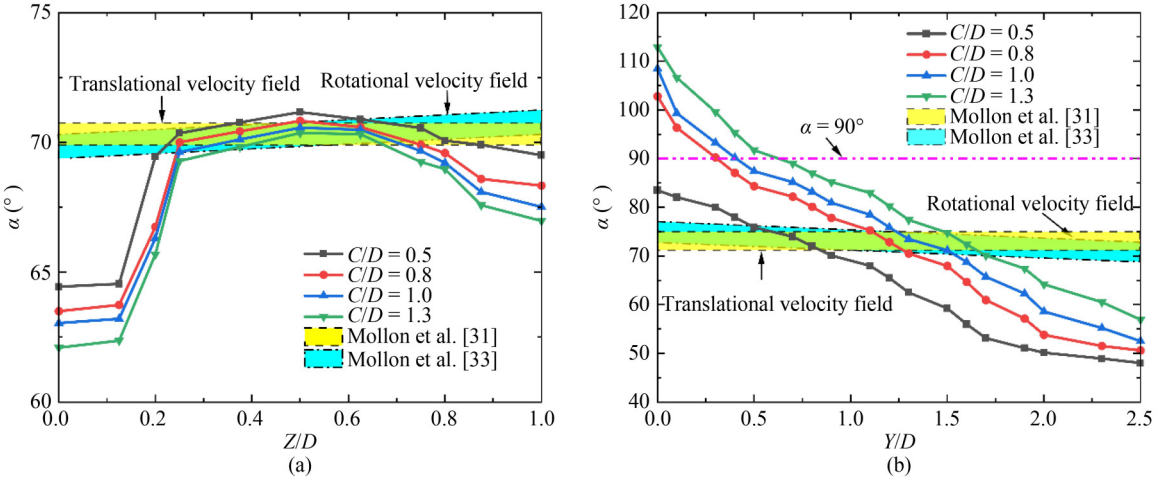

Fig. 16 Velocity field inclination in all cases: (a) at the tunnel face; (b) at the ground surface.

approximated by patterns of an oblique cone and an ellipsoidal arch, respectively. Hence, the inclination range of the translational and rotational velocity fields under different burial depth ratios was calculated. The velocity field of numerical simulations was compared with the translational and rotational velocity fields usually adopted in the existing analytical approaches. As shown in Fig. 16(a), the velocity inclination calculated through numerical simulation is consistent with the results of the rotational velocity field, indicating that the rotational velocity field correctly predicts the distribution of velocity fields at the tunnel face. It should be noted that the grid points lie within the undisturbed soil zone when Z/D < 0.2 and Z/D < 0.8, so the velocity inclinations of these undisturbed points differ from those of the other points; however, the translational velocity field has the unchanged velocity inclination, which oversimplifies the motion characteristics of the sand in front of the tunnel face. Hence, the double-logarithmic spiral mechanism established by Ref. [33] can reconstruct the failure model in front of such tunnel faces. As shown in Fig. 16(b), the velocity inclination α at the ground surface generally decreases as the Y/D value increases. As illustrated in Fig. 16(b), the slope of the inclination curves in the rotational velocity field was closer to the numerical simulation results only when C/D was 0.5. The finding indicated that the rotational velocity field cannot precisely describe the movement of the sand in the vicinity of the ground surface. In addition, the constant velocity inclination of the translational velocity field at the tunnel face was in line with the numerical result. However, the translational velocity field failed to characterize the variation of the velocity field at the ground surface. In conclusion, the marked line (α = 90°) in Fig. 16(b) was the dividing line of the velocity inclination α. The velocity inclination α below the marked line (α = 90°) was less than 90° when C/D = 0.5, hinting that the velocity field at the ground surface was not expanded. However, the velocity inclination was greater than 90° in the range of 0 to 0.75D at the ground surface above the marked line (α = 90°) when C/D = 0.8, 1, and 1.3, indicating that velocity fields expanded close

to the ground surface. Therefore, the formation of the extended upper failure zone was mainly caused by the expansion of the velocity field. Since the ground surface could be regarded as an unconstrained boundary, the soil arch did not develop beyond the ground surface for appropriately shallow tunnels (i.e., C/D = 0.8, 1, and 1.3). The stress of the soil on the ground surface was first relieved, resulting in the expansion of velocity fields when the soil arch developed upwards.

5 Limitation

The experimental equipment designed and used in this work to investigate the instability behavior of tunnel faces offers various advantages in terms of understanding the failure zone distribution of the passive instability of tunnel faces. However, the factor influencing the thickness of the upper failure zone was not clearly defined, and this was a limitation in this study. Although such factors were not central to this investigation, they will be explored in more detail in future work.

In summary, two main reasons for somewhat limiting the present work were that the length of the article was finite and the improved experiment was time-consuming; however, given that the main objective of this work was to evaluate the passive stability of shallow tunnel faces in coastal backfill sands through model tests, this limitation does not affect the ultimate evaluation. This work still has reference value for practical engineering.

6 Conclusions

To investigate the passive failure feature of tunnel faces for shallow shield tunnels in coastal backfill sand, an improved experiment was proposed, to perform four groups of 1–g small-scale model tests for different burial depth ratios (C/D = 0.5, 0.8, 1, and l.3). The variation of the face support pressure, the evolution of face failure processes, the geometry of face failure modes, and the distribution of velocity fields were analyzed. The main conclusions of this work are as follows.

1) The change in support pressures versus face displacements could be divided into four stages when C/D = 0.8, 1, and 1.3: there was a sharp rise in the support pressure, a gradual rise to a maximum value, a slight decrease, and a quasi-stable state. The decrease did not occur when C/D = 0.5, which indicated that a small burial depth ratio (C/D) was more likely to cause face blow-out of shield tunnels.

2) The contour of the failure zone showed a wedge-shaped arch when C/D = 0.5, which was mainly caused by the shear failure of the sand; the final shape of failure zones consisted of both the arch and the inverted trapezoid when C/D = 0.8, 1, and 1.3, in which the failure zone could be divided into lower and upper zones. The shear failure in front of such tunnel faces led to the formation of the lower failure zone, and the upper failure zone was formed by soil stress relief on the ground surface.

3) Comparing experimental and numerical results, the variation trends of support pressures and the range of failure zones were approximately consistent. The expansion of the velocity field at the ground surface led to the extension of the upper failure zone when C/D = 0.8, 1, and 1.3. Additionally, the classical velocity field model could simulate the velocity field distribution ahead of tunnel faces, but it could not reflect the velocity field distribution at the ground surface.

Appendix A

The friction between the piston and the tunnel in model tests led to the non-uniformity of the support pressure and face displacement. Kirsch [51] suggested that reference measurements made with hydrostatic pressure were employed to quantify the friction within the whole system, thus weakening the effect of non-uniformity on support pressures. The strategy of reference measurements was to maintain a constant load as the piston movement. In this process, a difference between applied and measured pressure could be interpreted as the effect of non-uniformity. The force acting on the piston was defined by the standard support pressure, and the pressure obtained from the earth pressure cell was the measured support pressure. Similarly, in the process of reference measurements, the standard and measured displacements could be determined, respectively. As shown in Fig. A1, the test data output from sensors was steady, and the linear fitting method was able to modify the test data to weaken the effect of non-uniformity.

Appendix B

Two model tests with C/D = 0.6 and 0.7 were conducted for simple observation. The failure patterns obtained from model tests are shown in Fig. A2. Comparing with the results of C/D = 0.5, it can be seen that the failure mode with C/D = 0.6 and 0.7 has the upper and lower failure zone, indicating that the failure modes C/D = 0.5 and 0.6 were generally consistent with those of C/D = 0.8, 1, and 1.3.

Acknowledgements This work was supported by the National Natural Science Foundation of China (Grant No. 41972276), the Natural Science Foundation of Fujian Province (No. 2020J06013), and the “Foal Eagle Program” Youth Top-notch Talent Project of Fujian Province (No. 00387088). This financial support is gratefully acknowledged.

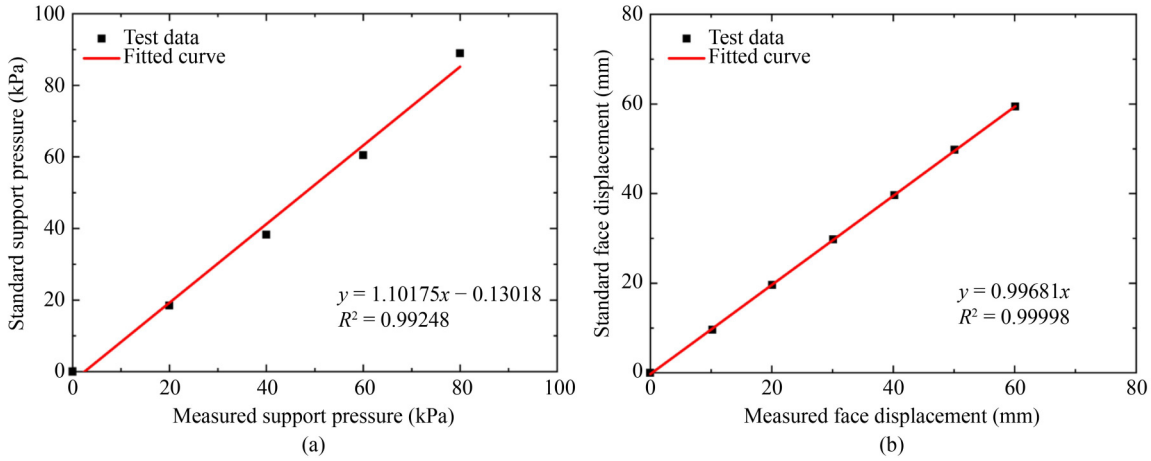

Fig. A1 Example of sensor calibration curves: (a) earth pressure cell; (b) displacement sensor.

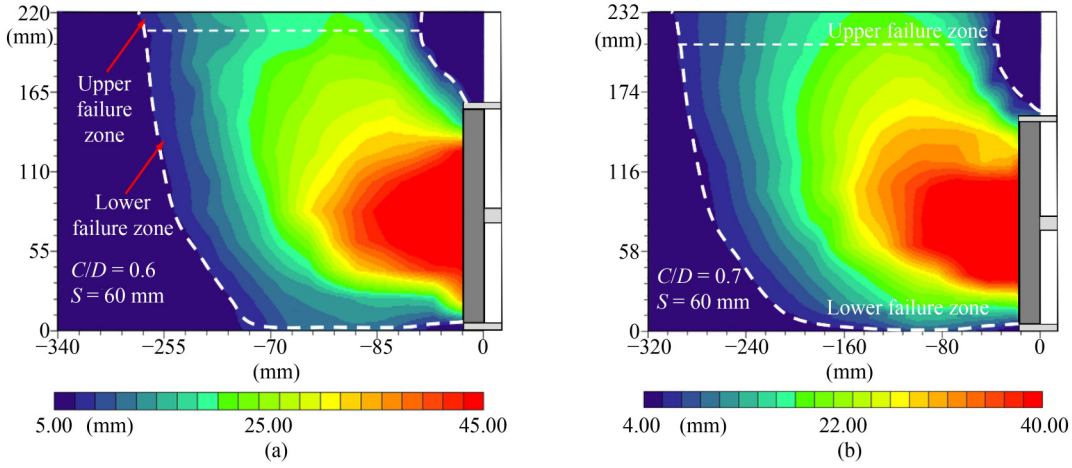

Fig. A2 Displacement fields of sand for different burial depth ratios *C*/*D*: (a) 0.6; (b) 0.7.

Competing interests The authors declare that they have no competing interests.

References

1. Guglielmetti V, Grasso P, Mahtab A, Xu S L. Mechanized Tunneling in Urban Areas: Design Methodology and Construction Control. London: Taylor and Francis, 2008, 2–14
2. Qian W F, Huang M, Sun C M, Huang B, Wang G F, Liu H. Adaptability of earth pressure balance shield tunneling in coastal complex formations: A new evaluation method. Geomechanics and Engineering, 2021, 27: 425−440
3. Liao S, Liu J, Wang R, Li Z. Shield tunneling and environment protection in Shanghai soft ground. Tunnelling and Underground Space Technology, 2009, 24: 454−465
4. Sterpi D, Rizzo F, Renda D, Aguglia F, Zenti C. Soil nailing at the tunnel face in difficult conditions: A case study. Tunnelling and Underground Space Technology, 2013, 38: 129−139
5. Chen R P, Yin X, Tang L, Chen Y. Centrifugal model tests on face failure of earth pressure balance shield induced by steady state seepage in saturated sandy silt ground. Tunnelling and Underground Space Technology, 2018, 81: 315−325
6. Yin Z Y, Wang P, Zhang F S. Effect of particle shape on the progressive failure of shield tunnel face in granular soils by coupled FDM-DEM method. Tunnelling and Underground Space Technology, 2020, 100: 103394
7. Chen R P, Li J, Kong L G, Tang L J. Experimental study on face instability of shield tunnel in sand. Tunnelling and Underground Space Technology, 2013, 33: 12−21
8. Sun X H, Miao L C, Lin H S, Tong T Z. Soil arch effect analysis of shield tunnel in dry sandy ground. International Journal of Geomechanics, 2018, 18(6): 04018057
9. Liu W, Zhao Y, Shi P X, Li J Y, Gan P L. Face stability analysis of shield-driven tunnels shallowly buried in dry sand using 1–g large-scale model tests. Acta Geotechnica, 2018, 13(3): 693−705
10. Wong K S, Ng C W W, Chen Y M, Bian X C. Centrifuge and numerical investigation of passive failure of tunnel face in sand. Tunnelling and Underground Space Technology, 2012, 28(3): 297−303
11. Ng C W W, Wong K S. Investigation of passive failure and deformation mechanisms due to tunneling in clay. Canadian Geotechnical Journal, 2013, 50(4): 359−372
12. Liu W, Shi P X, Chen L J, Tang Q. Analytical analysis of working

face passive stability during shield tunneling in frictional soils. Acta Geotechnica, 2020, 15(3): 781−794
13. Klotz U, Vermeer P, Klotz C, Möller S. A 3D finite element simulation of a shield tunnel in weathered Singapore Bukit Timah granite. Tunnelling and Underground Space Technology, 2006, 21(3−4): 272
14. Bezuijen A, Brassinga H M. Tunneling. A Decade of Progress. GeoDelft. London: Taylor and Francis, 2005, 143–148
15. Qi L Z. Study on blow-out face pressure of shield tunnels in sand. Thesis for the Master's Degree. Hangzhou: Zhejiang University, 2012 (in Chinese)
16. GB 50157-2013. Code for Design of Metro. Beijing: Ministry of Housing and Urban-Rural Development of the People's Republic of China, 2013 (in Chinese)
17. Li P F, Chen K Y, Wang F, Li Z. An upper-bound analytical model of blow-out for a shallow tunnel in sand considering the partial failure within the face. Tunnelling and Underground Space Technology, 2019, 91: 102989
18. Xu K, Huang M, Zhen J J, Xu C S, Cui M J. Field implementation of enzyme-induced carbonate precipitation technology for reinforcing a bedding layer beneath an underground cable duct. Journal of Rock Mechanics and Geotechnical Engineering, 2023, 15: 1011−1022
19. Horn N. Horizontal earth pressure on perpendicular tunnel face. In: Proceedings of the Hungarian National Conference of the Foundation Engineer Industry. Budapest: Akadémiai Kiadó, 1961, 7–16 (in Hungarian)
20. Broere W. Tunnel face stability and new CPT applications. Dissertation for the Doctoral Degree. Delft: Delft University of Technology, 2001
21. Hu X Y, Zhang Z X, Kieffer S. A real-life stability model for a large shield-driven tunnel in heterogeneous soft soils. Frontiers of Structural and Civil Engineering, 2012, 6(2): 176−187
22. Perazzelli P, Leone T, Anagnostou G. Tunnel face stability under seepage flow conditions. Tunnelling and Underground Space Technology, 2014, 43: 459−469
23. Anagnostou G, Perazzelli P. Analysis method and design charts for bolt reinforcement of the tunnel face in cohesive-frictional soils. Tunnelling and Underground Space Technology, 2015, 47: 162−181
24. Chen R P, Tang L J, Yin X S, Chen Y M, Bian X C. An improved 3D wedge-prism model for the face stability analysis of the shield tunnel in cohesionless soils. Acta Geotechnica, 2015, 10: 683−692
25. Huang M, Zhan J W. Face stability assessment for underwater tunneling across a fault zone. Journal of Performance of Constructed Facilities, 2019, 33(3): 04019034
26. Zhang X, Wang M N, Li J W, Wang Z L, Tong J J, Liu D G. Safety factor analysis of a tunnel face with an unsupported span in cohesive-frictional soils. Computers and Geotechnics, 2020, 117: 103221
27. Zhang X, Wang M N, Wang Z L, Li J W, Tong J J, Liu D G. A limit equilibrium model for the reinforced face stability analysis of a shallow tunnel in cohesive-frictional soils. Tunnelling and Underground Space Technology, 2020, 105: 103562
28. Cheng C, Ni P, Zhao W, Jia P, Gao S, Wang Z, Deng C. Face stability analysis of EPB shield tunnel in dense sand stratum considering the evolution of failure pattern. Computers and Geotechnics, 2021, 130: 103890
29. Leca E, Dormieux L. Upper and lower bound solutions for the face stability of shallow circular tunnels in frictional material. Geotechnique, 1990, 40(4): 581−606
30. Soubra A H, Dias D, Emeriault F, Kastner R. Three-dimensional face stability analysis of circular tunnels by a kinematical approach. In: Proceedings of GeoCongress 2008: Characterization, Monitoring, and Modeling of GeoSystems. New Orleans: ASCE, 2008: 894–901
31. Mollon G, Dias D, Soubra A H. Face stability analysis of circular tunnels driven by a pressurized shield. Journal of Geotechnical and Geoenvironmental Engineering, 2010, 136(1): 215−229
32. Mollon G, Dias D, Soubra A H. Probabilistic analysis of pressurized tunnels against face stability using collocation-based stochastic response surface method. Journal of Geotechnical and Geoenvironmental Engineering, 2011, 137(4): 385−397
33. Mollon G, Dias D, Soubra A H. Rotational failure mechanisms for the face stability analysis of tunnels driven by a pressurized shield. International Journal for Numerical and Analytical Methods in Geomechanics, 2011, 35(12): 1363−1388
34. Tang X W, Liu W, Albers B, Savidis S. Upper bound analysis of tunnel face stability in layered soils. Acta Geotechnica, 2014, 9(4): 661−671
35. Zhang C P, Han K H, Zhang D L. Face stability analysis of shallow circular tunnels in cohesive-frictional soils. Tunnelling and Underground Space Technology, 2015, 50: 345−357
36. Pan Q J, Dias D. Safety factor assessment of a tunnel face reinforced by horizontal dowels. Engineering Structures, 2017, 142: 56−66
37. Ding W T, Liu K Q, Shi P H, Li M J, Hou M L. Face stability analysis of shallow circular tunnels driven by a pressurized shield in purely cohesive soils under undrained conditions. Computers and Geotechnics, 2019, 107: 110−127
38. Li P F, Wei Y J, Zhang M J, Huang Q F, Wang F. Influence of non-associated flow rule on passive face instability for shallow shield tunnels. Tunnelling and Underground Space Technology, 2022, 119: 104202
39. Di Q D, Li P F, Zhang M J, Zhang W J, Wang X Y. Analysis of face stability for tunnels under seepage flow in the saturated ground. Ocean Engineering, 2022, 266: 112674
40. Di Q D, Li P F, Zhang M J, Guo C X, Wang F, Wu J. Three-dimensional theoretical analysis of seepage field in front of shield tunnel face. Underground Space, 2022, 7(4): 528−542
41. Ukritchon B, Yingchaloenkitkhajorn K, Keawsawasvong S. Three-dimensional undrained tunnel face stability in clay with a linearly increasing shear strength with depth. Computers and Geotechnics, 2017, 88: 146−151
42. Ding X B, Li K, Xie Y X, Liu S Z. Face stability analysis of large shield-driven tunnel in rock−soil interface composite formations. Underground Space, 2022, 7(6): 1021−1035
43. Li W, Zhang C P, Zhang D L, Ye Z J, Tan Z B. Face stability of shield tunnels considering a kinematically admissible velocity field of soil arching. Journal of Rock Mechanics and Geotechnical Engineering, 2022, 14(2): 505−526
44. Senent S, Jimenez R. A tunnel face failure mechanism for layered

ground, considering the possibility of partial collapse. Tunnelling and Underground Space Technology, 2015, 47: 182−192
45. Chen R P, Tang L, Ling D, Chen Y. Face stability analysis of shallow shield tunnels in dry sandy ground using the discrete element method. Computers and Geotechnics, 2011, 38(2): 187−195
46. Zhang Z, Hu X, Scott K. A discrete numerical approach for modeling face stability in slurry shield tunneling in soft soils. Computers and Geotechnics, 2011, 38(1): 94−104
47. Zhang Z H, Xu W S, Nie W T, Deng L M. DEM and theoretical analyses of the face stability of shallow shield cross-river tunnels in silty fine sand. Computers and Geotechnics, 2021, 130: 103905
48. Chambon P, Corté J F. Shallow tunnels in cohesionless soil: Stability of tunnel face. Journal of Geotechnical Engineering, 1994, 120(7): 1148−1165
49. Idinger G, Aklik P, Wu W, Borja R I. Centrifuge model test on the face stability of shallow tunnel. Acta Geotechnica, 2011, 6(2): 105−117
50. Weng X L, Sun Y F, Yan B H, Niu H S, Lin R A, Zhou S Q. Centrifuge testing and numerical modeling of tunnel face stability considering longitudinal slope angle and steady state seepage in soft clay. Tunnelling and Underground Space Technology, 2020, 101: 103406
51. Kirsch A. Experimental investigation of the face stability of shallow tunnels in sand. Acta Geotechnica, 2010, 5(1): 43−62
52. Berthoz N, Branque D, Subrin D, Wong H, Humbert E. Face failure in homogeneous and stratified soft ground: theoretical and experimental approaches on 1g EPBS reduced scale model. Tunnelling and Underground Space Technology, 2012, 30: 25−37
53. Di Q D, Li P F, Zhang M J, Cui X P. Influence of relative density on deformation and failure characteristics induced by tunnel face instability in sandy cobble strata. Engineering Failure Analysis, 2022, 141: 106641
54. Di Q D, Li P F, Zhang M J, Cui X P. Experimental study of face stability for shield tunnels in sandy cobble strata of different densities. Tunnelling and Underground Space Technology, 2023, 135: 105029
55. Di Q D, Li P F, Zhang M J, Cui X P. Experimental investigation of face instability for tunnels in sandy cobble strata. Underground Space, 2023, 10: 199−216
56. Cheng C, Jia P J, Zhao W, Ni P P, Bai Q, Wang Z J, Lu B. Experimental and analytical study of shield tunnel face in dense sand stratum considering different longitudinal inclination. Tunnelling and Underground Space Technology, 2021, 113: 103950
57. Zhang X, Wang M, Lyu C, Tong J, Yu L, Liu D. Experimental and numerical study on tunnel faces reinforced by horizontal bolts in sandy ground. Tunnelling and Underground Space Technology, 2022, 123: 104412
58. Lei H Y, Zhang Y J, Hu Y, Liu Y N. Model test and discrete element method simulation of shield tunneling face stability in transparent clay. Frontiers of Structural and Civil Engineering, 2021, 15(1): 147−166
59. Ma S K, Duan Z B, Huang Z, Liu Y, Shao Y. Study on the stability of shield tunnel face in clay and clay-gravel stratum through large-scale physical model tests with transparent soil. Tunnelling and Underground Space Technology, 2022, 119: 104199
60. Lü X L, Zhou Y C, Huang M S, Zeng S. Experimental study of the face stability of shield tunnel in sands under seepage condition. Tunnelling and Underground Space Technology, 2018, 74: 195−205
61. Jia Z, Bai Y T, Liu C, Zhang D S, Ji Y P, Zhao H H. Visualization investigation on stability of shield tunnel face with transparent soil, considering different longitudinal inclination angles. Tunnelling and Underground Space Technology, 2023, 137: 105154
62. Saiyar M, Ni P, Take W A, Moore I D. Response of pipelines of differing flexural stiffness to normal faulting. Geotechnique, 2016, 66(4): 275−286
63. Tognon A R, Rowe R K, Brachman R W I. Evaluation of side wall friction for a buried pipe testing facility. Geotextiles and Geomembranes, 1999, 17(4): 193−212
64. TB 10001-2016. Technical Code for Design of Railway Tunnel. Beijing: National Railway Administration of People's Republic of China, 2016 (in Chinese)
65. Fang Q, Liu X, Zeng K H, Zhang X D, Zhou M Z, Du J M. Centrifuge modelling of tunneling below existing twin tunnels with different types of support. Underground Space, 2022, 7(6): 1125−1138
66. Gioda G, Swoboda G. Developments and applications of the numerical analysis of tunnels in continuous media. International Journal for Numerical and Analytical Methods in Geomechanics, 1999, 23(13): 1393−1405